Progress in Natural Science: Materials International xxx (xxxx) xxx–xxx

HOSTED BY

ELSEVIER

Contents lists available at ScienceDirect

Progress in Natural Science: Materials International

journal homepage: www.elsevier.com/locate/pnsmi

Original Research

Phase formation of a biocompatible Ti-based alloy under kinetic constraints studied via *in-situ* high-energy X-ray diffraction

Konrad Kosiba[a,*], André Rothkirch[b], Junhee Han[c], Liang Deng[a], Benjamin Escher[d], Gang Wang[e], Uta Kühn[a], Jozef Bednarcik[f]

[a] Leibniz IFW Dresden, Institute for Complex Materials, Helmholtzstraße 20, 01069, Dresden, Germany
[b] DESY Photon Science, Notkestraße 85, D-22607, Hamburg, Germany
[c] Korea Institute of Industrial Technology (KITECH), Korea Institute for Rare Metals, 156, Gaetbeol-ro, Yeonsu-gu, 21999, Incheon, South Korea
[d] Fraunhofer Institute for Photonic Microsystems IPMS, Department of Engineering, Maria-Reiche-Str. 2, 01109, Dresden, Germany
[e] Laboratory for Microstructures, Institute of Materials, Shanghai University, Shanghai, 200444, China
[f] J. Safarik University in Kosice, Institute of Physics, Department of Condensed Matter Physics, Park Angelinum 9, 04154, Kosice, Slovakia

ARTICLE INFO

Keywords:
High-energy X-ray diffraction
Flash-annealing
Phase formation
Metallic glass
Biocompatible Ti alloy

ABSTRACT

The biocompatible $Ti_{40}Cu_{34}Pd_{14}Zr_{10}Sn_2$ bulk metallic glass was rapidly heated, also known as flash-annealed, at varying heating rates up to 1579 K/s. Thereby, the phase formation was characterized via advanced *in-situ* high-energy X-ray diffraction. It has been found that the evolving kinetic constraints can be used as a tool to deliberately alter the crystalline phase formation. This novel processing route permits to select phases to crystallize to a predefined fraction and, thus, to potentially design the microstructure of materials according to a specified property-profile. Consequently, flash-annealing poses a unique synthesis route to design materials with, for instance, good biomechanical compatibility.

1. Introduction

The design of advanced metallic materials is given special attention as bone replacement implants. In particular, Ti-based alloys represent excellent biomaterials for long-term implantation due to good fatigue resistance, excellent biological passivity and especially biomechanical compatibility, which depends on the match of Young's moduli from the bone (about 30 GPa) and the implant [1–6]. When the implant has an incomparable higher Young's modulus, *E*, it takes over a considerable part of the loading and, hence, shields the bone from the necessary stressing required to maintain its strength, density, and healthy structure. This effect is known in literature as "stress-shielding", can lead to resorption of the bone in the vicinity of the implant and ultimately to premature failure of the implant or its loosening [3,4,7,8].

Compared to commercially used metallic implant materials, like 316L stainless steel (210 GPa) [9], Ti-based alloys show distinctly lower Young's moduli, which strongly depend on the phase(s) comprising the microstructure. $\alpha-$ Ti-based alloys have an *E* of about 110 GPa [10], whereby the *E* of metastable $\beta-$Ti ranges from about 80 GPa down to even 42 GPa [11] being quite close to that of bone (about 30 GPa) [4]. Owing to the resulting low mismatch of *E*, metastable $\beta-$Ti alloys are recently in the focus of intense research. They are prepared by casting at high cooling rates [12]. If the melt is quenched even faster, crystallization can be fully or only partially circumvented entailing the synthesis of, for example, biocompatible Ti-based bulk metallic glasses (BMGs) [13,14] and composites [15], respectively. BMGs also show low *E*, high corrosive resistance, but also very limited plastic deformability posing their Achilles heel. A very effective way to attenuate their brittle behavior is to incorporate crystals into the glass, so that the resulting BMG composites additionally exhibit plastic deformability [16–19]. Thereby, it is important to prepare composites with uniformly distributed crystals, but this is very challenging with the current standard preparation method – melt-quenching [19–22]. So far, BMG composites with uniformly distributed crystals can be prepared by melt-quenching only for a scarce number of glass-forming alloys [23,24]. Furthermore, it is impossible to deliberately select the type of crystalline phase(s) (given by the chemical composition) to precipitate during cooling within the supercooled liquid. Yet, it is pivotal to synthesize biomechanical compatible implant material in a controlled manner, since the phase(s) and corresponding chemical composition determine(s) *E* and thus its biomechanical compatibility [1,3,4,8,25,26].

Flash-annealing of BMGs provides an alternative processing route to overcome these limitations in synthesizing, besides others, advanced BMG composites [27,28]. Upon heating, the glass firstly transforms into

* Corresponding author.
E-mail address: k.kosiba@ifw-dresden.de (K. Kosiba).

https://doi.org/10.1016/j.pnsc.2020.06.004
Received 9 March 2020; Received in revised form 10 June 2020; Accepted 11 June 2020

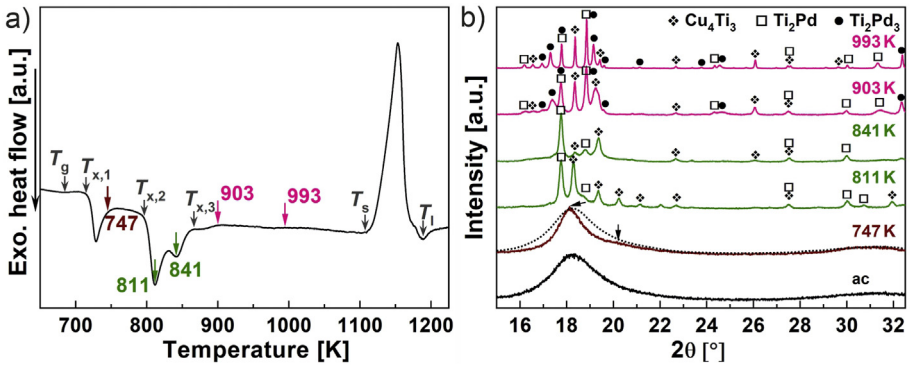

Fig. 1. Phase formation of the $Ti_{40}Cu_{34}Pd_{14}Zr_{10}Sn_2$ glass-forming alloy without kinetic constraints. a) High-temperature DSC trace at 20 K/min. The characteristic temperatures are indicated: glass-transition temperature (T_g), crystallization temperatures ($T_{x,1}$, $T_{x,2}$, $T_{x,3}$), solidus temperature (T_s), and liquidus temperature (T_l). b) Ex-situ XRD patterns of the $Ti_{40}Cu_{34}Pd_{14}Zr_{10}Sn_2$ BMG heated to 747, 811, 841, 903 and 993 K. In addition, the pattern prior to heating (as-cast; ac) is shown. The dotted line on top of the pattern of 747 K is an overlay of the ac pattern to allow for easier comparison.

the supercooled liquid which crystallizes later on. By varying the heating rate, different crystalline phase regions can be accessed. Consequently, this envisaged processing route enables the controlled synthesis of BMG-composites or even novel metastable fully crystalline materials [27]. In order to design the microstructure, one must firstly identify the phase formation dependent on the heating rate and this is the focus of the present work. Here, we heated a $Ti_{40}Cu_{34}Pd_{14}Zr_{10}Sn_2$ bulk metallic glass [29], which is expected to be biocompatible [13], at five heating rates ranging from 0.3 K/s to 1579 K/s and studied the phase formation via *in-situ* high-energy X-ray diffraction. The phase regions are identified dependent on temperature and time with high temporal resolution permitting to construct the continuous heating transformation (CHT) diagram of this biocompatible Ti-based alloy. We demonstrate that our *in-situ* HEXRD setup allows resolving extremely fast occurring structural changes under kinetic constraints. We explore the suppression of equilibrium phases and/or formation of metastable phases which could be potentially biomechanical compatible.

2. Experimental

Pre-alloys of $Ti_{40}Cu_{34}Pd_{14}Zr_{10}Sn_2$ were prepared from high-purity elements (purity ≥ 99.99%) by arc-melting in a Ti-gettered Ar-atmosphere. Each ingot with a mass of about 25 g was re-melted three times to ensure chemical homogeneity. Pieces of the ingots were used to produce plates (10 mm × 1.5 mm x 55 mm) via suction casting in a water-cooled copper mold (Edmund Bühler) also under Ar-atmosphere. Afterwards they were sliced into 10 mm long pieces. Prior to characterization, the specimens were grinded down to a uniform thickness, so that their final geometry is: 10 mm × 1.5 mm x 0.5 mm.

Thermal analysis was carried out in differential scanning calorimeter (DSC) (Netzsch 404 C) at a heating rate of 20 K/min up to 1273 K in Al_2O_3-crucibles under argon atmosphere to determine the glass-transition temperature T_g, crystallization temperatures $T_{x1,2,3}$, the solidus temperature T_s and the liquidus temperature T_{liq} at near-equilibrium conditions.

Structural characterization was carried out *ex-situ* by X-ray diffraction (XRD) using a STOE STADI P with Mo-$K_{\alpha 1}$ radiation (λ = 0.7093 Å). In order to investigate the phase formation at faster heating rates up to 1579 K/s, *in-situ* high-energy X-ray diffraction (HEXRD) was carried out at the P02.1 beamline at the Deutsches Elektronen-Synchrotron (DESY) (wavelength 0.2066 Å and beam size 500 µm × 500 µm). Diffraction patterns were recorded using the 2D Lambda 2 M GaAs detector (X-Spectrum, pixel size 55 µm × 55 µm) at frame rates of 100 and 200 Hz and a sample-to-detector distance of 248 mm. The 2D patterns were integrated using the DESY p02_processingtool software package, developed by one of the authors, and quantified by means of GNU Octave. The specimens were heated inside a measuring chamber developed at the IFW Dresden via an electrical current pulse generated by a power supply unit (Magna-Power SL 25–60 equipped with the Option + HS 1,5–15) connected to a signal wave generator (Rohde & Schwarz HMF2525). The surface temperature of the specimens was monitored by a pyrometer (Lumasense IGAR 12LO, 500 Hz), which was previously calibrated using a type T thermocouple. The electrical current was measured by a current probe (Chauvin Arnoux E3) with switching electronics which transform it into a voltage signal. A data logger (FLUKE NetDAQ 2645A, 1000 Hz) was utilized to record the temperature, electrical current and voltage signals.

3. Results

3.1. Phase evolution without kinetic constraints

In order to study the phase formation of the $Ti_{40}Cu_{34}Pd_{14}Zr_{10}Sn_2$ BMG under kinetic constraints, its phase formation without such constraints was firstly characterized to obtain a reference state. Such a study was already carried out for the $Ti_{40}Cu_{36}Pd_{14}Zr_{10}$ BMG [30] which is very similar in composition to the present alloy and thus should facilitate the phase analysis. Fig. 1a depicts the DSC curve of the BMG. Upon heating, the glass firstly devitrifies at the glass transition at which it transformed into a supercooled liquid. This transformation was indicated by the glass-transition temperature T_g. With further heating, crystallization (marked by a distinct exothermic event) set in at the crystallization temperature T_x [31]. For the present BMG, three exothermic events were detected. After the crystallization of the supercooled liquid, it begins to melt once the solidus temperature T_s was passed during heating. Only the liquid was present above the liquidus temperature T_l. The $Ti_{40}Cu_{34}Pd_{14}Zr_{10}Sn_2$ supercooled liquid sequentially crystallized into different phases [29]. In order to identify these phases, identical samples were heated to five characteristic temperatures (Fig. 1a: 747, 811, 841, 903 and 993 K), subsequently cooled at about 100 K/min and *ex-situ* analyzed by XRD. Fig. 1b displays the corresponding patterns. Prior to heating, the BMG was fully amorphous as confirmed by the respective XRD pattern (Fig. 1b: black curve, ac). Only broad maxima were visible in the pattern, but no sharp reflections corresponding to crystalline phase(s) could be observed. The XRD pattern of the sample heated to 747 K, after the first crystallization event was completed, also did not show any sharp reflections. Instead a broader maximum with less pronounced convexity was present (Fig. 1b, marked by two arrows). The first maximum was narrower and altogether sharper, compared to the as-cast curve which is superposed on it (Fig. 1b: brown curve superposed by black dotted curve). One reason for it could result from structural relaxation. Since the supercooled liquid only partially crystallized when heated to 747 K, subsequent cooling occurred at distinctly lower cooling rates (1.7 K/s) than during the preparation of the BMG via melt-quenching. Thus less free volume was trapped during re-vitrification of the residual supercooled liquid [32]. The resulting structure of the amorphous volume fraction was then more relaxed characterized by a lower number of different interatomic distances which is again reflected in a lower width of the first diffraction maximum [33,34]. However, it should only narrow to a lesser extent than observed in Fig. 1b [35]. Therefore, another and

more likely reason for the narrowing seems to be thermally induced nanocrystallization, which also occurred at the closely related $Ti_{40}Cu_{36}Pd_{14}Zr_{10}$ BMG when heated to similar temperatures. Thereby, the Cu_4Ti_3 phase (*I4/mmm*) [36] crystallized on a nanometer scale [30]. The volume fraction of these nanocrystals increased when further heated and they also grow in size permitting to confirm their presence via XRD [30]. After heating another specimen to higher temperatures of 811 and 841 K (Fig. 1b: green curves), the presence of this already suspected nanocrystalline Cu_4Ti_3 phase can be confirmed and additionally the Ti_2Pd phase (*I4/mmm*) crystallized [37]. The latter phase seems to form at the expense of Cu_4Ti_3 during the second crystallization event. At further heating, a less pronounced exothermic event followed at which the Ti_2Pd_3 phase (*Cmcm*) [38] formed (Fig. 1b: magenta curves, 903 and 993 K). All three crystalline phases were also forming when the closely related $Ti_{40}Cu_{36}Pd_{14}Zr_{10}$ BMG was heated [30].

3.2. Phase evolution under kinetic constraints

The phase formation of the $Ti_{40}Cu_{34}Pd_{14}Zr_{10}Sn_2$ glass-forming alloy was investigated under kinetic constraints which were imparted by fast heating with rates up to 1579 K/s. Thereby, very fast occurring structural changes could be only monitored and subsequently, analyzed *in-situ* via high-energy X-ray diffraction, because of the extremely high temporal resolution (200 Hz) of the utilized next generation detector. This unique and powerful experimental setup allows to investigate the phase formation dependent on time and temperature as well as to evaluate whether the forming phases are metastable. Therefore, identical BMG specimens were rapidly heated at 28, 226, 700 as well as 1579 K/s. Fig. 2a depicts the temperature and resistance as a function of time for the BMG heated at 28 K/s. Four distinct phase regions can be observed, indicated by vertical dashed lines.

The temperature-time (*T-t*) heating curve shows that at the beginning a constant slope until a first temperature increase at about 5.8 s can be observed (Fig. 2a, second dashed line). By contrast, the slope of the resistance-time curve slightly decreased already at 3.7s (723 K), as can be seen from the two linear fits (Fig. 2a, two grey lines). Since the resistivity of metallic glasses is slightly higher than that of the respective supercooled liquid, the intersection of both linear fits marks the glass-transition temperature T_g [39,40]. At further heating, the resistance distinctly drops at 5.8 s, coincides with the strong temperature increase and can be attributed to recalescence [27]. The reason is that the resistivity of the crystalline material is lower than of the corresponding supercooled liquid [41]. The temperature at the beginning of this strong increase marks the crystallization onset temperature $T_{x,1}$ (= 781 K). Once the first phase crystallized, the slope of the *T-t* curve diminishes and turns constant until a second steep temperature increase can be observed. This second crystallization event correlates with a second pronounced drop in resistance (t = 8.9 s, $T_{x,1}$ = 911 K). Both crystallization events can be verified via in-situ HEXRD. Only broad diffraction maxima were visible prior to the first crystallization event, typical for glass and supercooled liquids. At the onset of crystallization (Fig. 2a, left dashed line), the diffuse maxima transformed into sharp diffraction reflections. At the second crystallization event, the strong main reflection transformed into two weaker reflections. The changing intensity of the strongest peak reflects the structural change as a function of temperature, or rephrased both crystallization events, see Fig. 2b. The intensity of the first sharp reflection is much more intense than the broad maximum, so that the intensity-temperature curve steeply increases when crystallization sets in. At the second crystallization event, this first crystalline phase transforms into another one, since the strong single reflection is replaced by two major reflections with lower intensity. Consequently, the intensity-temperature curve also decreases. In order to identify the crystalline phases, representative diffraction patterns were analyzed. The patterns were normalized to allow accounting for weaker reflections and they are given in Fig. 2c. Prior to crystallization, the supercooled liquid was present and only broad diffraction maxima were visible in the corresponding HEXRD pattern (Fig. 2c, black). After the first crystallization, the HEXRD pattern at 857 K (Fig. 2c, green) showed sharp reflections which can be assigned to the Ti_2Pd phase (*I4/mmm*) [37]. The pattern recorded after the second crystallization event (Fig. 2c, magenta) proves the formation of Ti_2Pd_3 phase (*Cmcm*) [38]. Further heating experiments were carried out at 226, 700 as well as 1579 K/s and identical phases formed. At the highest heating rate, solely Ti_2Pd crystallized followed by melting. The characteristic temperatures of all heating rates are listed Table 1:

4. Discussion

The phase formation of the $Ti_{40}Cu_{34}Pd_{14}Zr_{10}Sn_2$ glass-forming alloy and how it is affected by kinetic constraints can be vividly discussed using a continuous heating transformation (CHT) diagram (Fig. 3). It is constructed from the characteristic temperatures, their change with heating rate and the phases formed. As known from literature [28,41], T_g and T_x increase with faster heating, so that the width of the

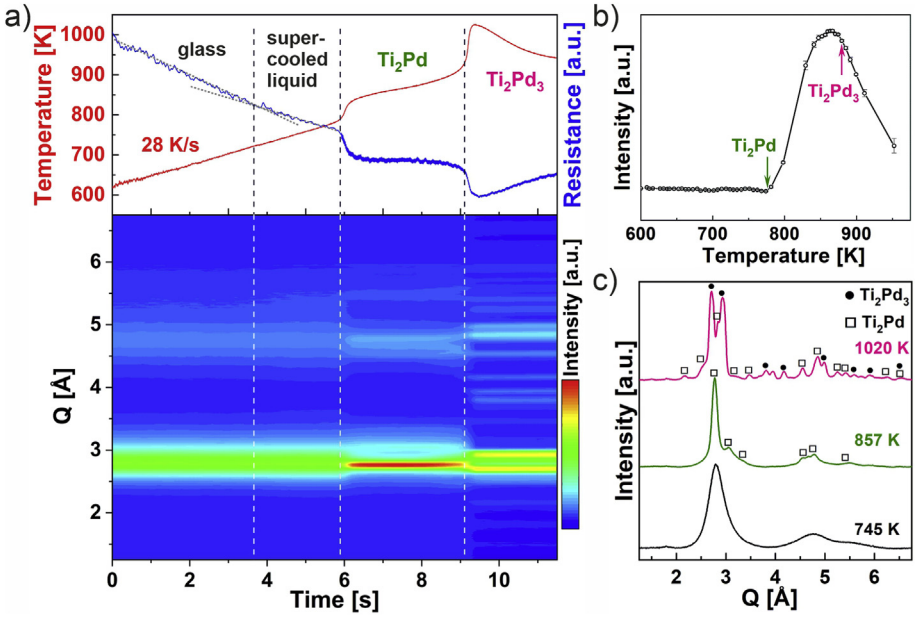

Fig. 2. Phase formation of the $Ti_{40}Cu_{34}Pd_{14}Zr_{10}Sn_2$ glass-forming alloy under kinetic constraints. a) Temperature and resistance of a BMG specimen heated at 28 K/s. Change in resistance from first to second regime is deduced from linear fitting (indicated by grey lines (top)). The corresponding projection of the diffraction intensity as a function of the wave vector Q and time is given at the bottom. b) Intensity of the strongest reflection dependent on temperature. c) Selected HEXRD patterns extracted from a) exemplifying the formation of the crystalline phases.

Table 1
Overview on the characteristic temperatures and the respective heating rates of flash-annealed $Ti_{40}Cu_{34}Pd_{14}Zr_{10}Sn_2$. The glass-transition temperature (T_g), crystallization temperatures ($T_{x,1,2,3}$) and liquidus temperature (T_l) are given. Note that two temperatures could not be determined from the data and they are marked with n.a. (not available).

Heating rate [K/s]	T_g [K]	T_{x1} [K]	T_{x2} [K]	T_{x3} [K]	T_l [K]
0.33 ± 0.01	677 ± 1	720 ± 1	800 ± 1	850 ± 1	1164 ± 10
28 ± 2	723 ± 10	781 ± 5	911 ± 5		1149 ± 20
226 ± 6	735 ± 10	809 ± 10	940 ± 30		n.a.
700 ± 11	747 ± 20	823 ± 10	945 ± 50		1154 ± 20
1579 ± 23	n.a.	893 ± 10			1155 ± 20

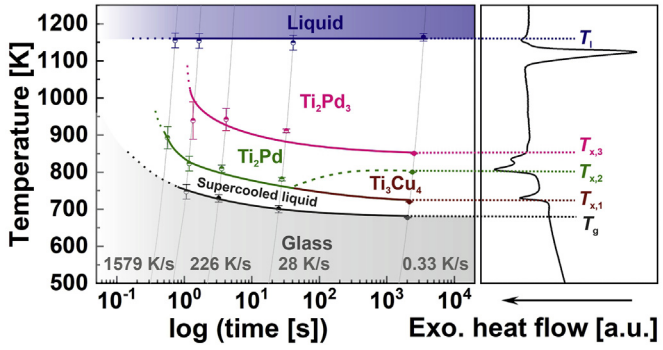

Fig. 3. Continuous-Heating-Transformation (CHT) diagram of the $Ti_{40}Cu_{34}Pd_{14}Zr_{10}Sn_2$ glass-forming alloy. The five heating rates and respective characteristic temperatures are indicated. Conditions without kinetic constraints are obtained from DSC (0.33 K/s) and the corresponding trace is shown on the right-hand side.

supercooled liquid widens. The phase formation without kinetic constraints is inferred from the DSC measurements (Fig. 3 right-hand side) which serve as starting point and, hence, will be addressed first.

As the supercooled liquid is heated above T_x, crystallization sets in. Crystallization proceeds by nucleation at which a solid-liquid interface is formed, and its advancement is termed crystal growth [42–44]. With increasing temperature, Ti_3Cu_4-nanocrystals firstly evolve from the supercooled liquid, so that high nucleation rates and distinctly lower crystal growth rates must be present at such large undercoolings. At further heating, Ti_2Pd crystallizes followed by Ti_2Pd_3, until melting sets in. Faster heating of the supercooled liquid at 28 K/s leads to the suppression of the Ti_3Cu_4 phase. Instead, Ti_2Pd is directly crystallizing from the supercooled liquid at temperatures where it should not be present under quasi-equilibrium conditions (Figs. 1 and 3) and is, thus, metastable. Its formation is not favored from a thermodynamic point of view, so that kinetic constraints must be responsible for it to crystallize at these temperatures. Thereby, the fast heating could hinder nucleation, crystal growth or both. As was shown for the B2 CuZr phase, which also directly crystallizes from a $Cu_{50}Zr_{50}$-based supercooled liquid at faster heating [28], time-dependent effects can play a pivotal role in the nucleation process at high heating rates. The critical radius, r^*, above which the nuclei are supercritical and continue to grow, increases at higher temperatures. At fast heating, the nuclei crystallize at higher temperatures and, moreover, have less time to exceed r^*. Thus, less B2 CuZr crystals form at higher heating rates above about 100 K/s [28]. For the present Ti_3Cu_4 phase, this effect is less likely, because nanocrystallization occurs [30], so that r^* appears to be very low. Moreover, this phase can be already suppressed at lower heating rates of 28 K/s. Consequently, the crystal growth of Ti_3Cu_4 must be strongly affected by fast heating in lieu of nucleation. All three phases crystallize primarily, where the chemical compositions of the crystalline phase and supercooled liquid differ. Primary crystallization is a typically diffusion-controlled process and involves a substantial incubation time [45]. When glasses, which subsequently transform into supercooled liquids, are subjected to rapid heating, atomic diffusion is limited [45]. The phase, whose crystal growth rate is less affected by the imparted kinetic constraints, begins to precipitate at temperatures where it is still metastable [27,28]. The incubation time for Ti_2Pd is then presumably shorter than for Ti_3Cu_4. Further heating at 28 K/s leads to the formation of the Ti_2Pd_3 phase. Thereby, one can observe that the corresponding T_x is augmenting with faster heating, until its formation is suppressed during flash-annealing at 1579 K/s (Fig. 3). Several reasons indicate that the crystallization of Ti_2Pd is kinetically favored over Ti_2Pd_3. The size of the unit cell of Ti_2Pd_3 (0.30644 nm^3 [38]) is more than three times larger than for Ti_2Pd (0,09586 nm^3 [37]), involves more atoms per unit cell and is also more complex from a crystallographic point of view. Thus, one can expect a larger r^* which nuclei of Ti_2Pd_3 must exceed in order to be supercritical. Owing to the more complex structure, also longer incubation times would result, so that the growth of the Ti_2Pd_3 phase can be more efficiently hampered by kinetic constraints.

The present results substantiate that different crystalline phase regions can be accessed by flash-annealing. If BMGs are heated at defined rates to preset temperatures followed by instantaneous quenching to preserve the microstructure present [27,28], then flash-annealing will permit to synthesize BMG composites or fully crystalline metastable metallic materials with preselected phases as well as volume fractions. The structure of all three crystalline phases is, of course, different and they also should yield microstructures with different Young's moduli. Flash-annealing poses an effective and novel processing method in synthesizing load-bearing implant material in a controlled manner, given an adequate alloy composition. However, our results and associated experimental work has shown that all crystalline phases formed for this alloy are rather brittle (not shown here). Thus, the resulting materials are not suitable for any use as implant, not to mention constructive material. Yet, the biocompatible $Ti_{40}Cu_{34}Pd_{14}Zr_{10}Sn_2$ glass-forming alloy represented a promising starting point for this study, since it is almost $Ti_{50}Cu_{50}$-based. We aimed to fathom the possibility of the more malleable TiCu or even α- or β-Ti phases to crystallize during flash-annealing at different heating rates. The lower Ti-content or rephrased higher fraction of the residual alloying elements of this alloy, which is vital for its high glass-forming ability [46], appears to not permit the TiCu, α- or β-Ti phases to be evolved based on a pure thermodynamic point of view. Although high kinetic constraints (up to 1579 K/s) are effective during flash-annealing, they cannot compensate for it. Particularly, β-Ti would be desirable because of its low Young's modulus and associated biomechanical compatibility with the human bone. The next step would be to repeat such a phase study with a different glass-forming composition with a higher Ti-content. Nevertheless, these results demonstrate the potential of this novel processing route to create microstructures and materials in a controlled manner. The associated properties, like for instance the biomechanical compatibility, could be designed following a predetermined profile using flash-annealing.

At last, we want to highlight the potential of the utilized *in-situ* HEXRD experimental setup. Fast occurring structural changes occur within the supercooled liquid during flash-annealing. They can lead to the formation of crystalline phases and could have been only monitored at very fast heating, owing to the extreme high temporal resolution of

this next-generation detector. Prior to crystallization, structural changes occur in the BMG as it relaxes, or rephrased densifies [47–49]. At further heating, it transforms into a supercooled liquid, whereby former frozen-in structural reconfigurations are active again. Subsequent fast cooling can even give rise to structural rejuvenation [47,48,50,51]. This *in-situ* HEXRD characterization technique, hence, represents a powerful tool to analyze the underlying structural changes during relaxation and rejuvenation, also under kinetic constraints.

5. Conclusions

The phase formation of the $Ti_{40}Cu_{34}Pd_{14}Zr_{10}Sn_2$ glass-forming alloy during fast heating at different heating rates ranging from 0.33 to 1579 K/s has been investigated via *in-situ* high-energy X-ray diffraction (HEXRD). Heating the bulk metallic glass (BMG) specimens at 0.33 K/s enables to investigate the phase formation without kinetic constraints. Thereby, the BMG firstly devitrifies into a supercooled liquid which sequentially crystallizes into the Ti_3Cu_4, Ti_2Pd and Ti_2Pd_3 phases during heating. With increasing heating rate, the formation of Ti_3Cu_4 and Ti_2Pd_3 is suppressed and a continuous heating transformation (CHT) diagram is constructed to illustrate it.

This work demonstrates that flash-annealing of glass-forming compositions at defined heating rates to predetermined temperatures followed by instantaneous quenching poses a unique tool to synthesize microstructures with preselected phases and volume fractions. Consequently, this novel processing route has the potential to literally design materials according to predetermined property-profiles, given a suitable alloy. Potential candidates could be Ti-based materials with low Young's moduli, which is a prerequisite for biomechanical compatibility. Next, one should identify an appropriate composition, where non-brittle phases can be accessed, as is in contrast to the investigated $Ti_{40}Cu_{34}Pd_{14}Zr_{10}Sn_2$ glass-forming alloy.

Declaration of competing interest

The authors declare that they have no known competing financial interests or personal relationships that could have appeared to influence the work reported in this paper.

Acknowledgements

Many thanks to S. Scudino for stimulating discussions. Financial support through the German Science Foundation (DFG) (grant: KO 5771/1–1) is acknowledged. Parts of this research were carried out at the light source PETRA III (beamline P02.1) at DESY, a member of the Helmholtz Association (HGF). Experimental support by K. Peukert, A. Horst, U. Biscop, H. Günther, D. Becker, S. Donath, N. Geißler, R. Keller and H. Merker is highly appreciated.

Appendix A. Supplementary data

Supplementary data to this article can be found online at https://doi.org/10.1016/j.pnsc.2020.06.004.

References

[1] M. Calin, A. Helth, J.J. Gutierrez Moreno, M. Bönisch, V. Brackmann, L. Giebeler, T. Gemming, C.E. Lekka, A. Gebert, R. Schnettler, J. Eckert, J. Mech. Behav. Biomed. Mater. 39 (2014) 162–174.
[2] A. Helth, S. Pilz, T. Kirsten, L. Giebeler, J. Freudenberger, M. Calin, J. Eckert, A. Gebert, J. Mech. Behav. Biomed. 65 (2017) 137–150.
[3] M. Geetha, A.K. Singh, R. Asokamani, A.K. Gogia, Prog. Mater. Sci. 54 (2009) 397–425.
[4] M.A.H. Gepreel, M. Niinomi, J. Mech. Behav. Biomed. 20 (2013) 407–415.
[5] G. He, M. Hagiwara, Mater. Sci. Eng. C 26 (2006) 14–19.
[6] L. Deng, S. Wang, P. Wang, U. Kühn, S. Pauly, Mater. Lett. 212 (2018) 346–349.
[7] R. Huiskes, H. Weinans, B. van Rietbergen, Clin. Orthop. Relat. Res. 274 (1992) 124–134.
[8] Q. Chen, G.A. Thouas, Mater. Sci. Eng. R 87 (2015) 1–57.
[9] M. Semlitsch, H.G. Willert, Med. Biol. Eng. Comput. 18 (1980) 511–520.
[10] Q. Liu, Q. Meng, S. Guo, X. Zhao, Nat. Sci. Mater. 23 (2013) 562–565.
[11] Y.L. Hao, S.J. Li, S.Y. Sun, C.Y. Zheng, R. Yang, Acta Biomater. 3 (2007) 277–286.
[12] A. Helth, P.F. Gostin, S. Oswald, H. Wendrock, U. Wolff, U. Hempel, S. Arnhold, M. Calin, J. Eckert, A. Gebert, J. Biomed. Mater. Res. B Appl. Biomater. 102 (2014) 31–41.
[13] A. Blanquer, E. Pellicer, A. Hynowska, L. Barrios, E. Ibáñez, M.D. Baró, J. Sort, C. Nogués, J. Mater. Sci. Mater. Med. 25 (2014) 163–172.
[14] S. Pang, Y. Liu, H. Li, L. Sun, Y. Li, T. Zhang, J. Alloys Compd. 625 (2015) 323–327.
[15] M. Calin, L.C. Zhang, J. Eckert, Scripta Mater. 57 (2007) 1101–1104.
[16] C.C. Hays, C.P. Kim, W.L. Johnson, Phys. Rev. Lett. 84 (2000) 2901-2901.
[17] D.C. Hofmann, J.-Y. Suh, A. Wiest, M.-L. Lind, M.D. Demetriou, W.L. Johnson, Proc. Natl. Acad. Sci. Unit. States Am. 105 (2008) 20136–20140.
[18] S. Pauly, J. Das, J. Bednarcik, N. Mattern, K. Kim, D. Kim, J. Eckert, Deformation-induced martensitic transformation in Cu–Zr–(Al,Ti) bulk metallic glass composites, Scripta Mater. 60 (2009) 431–434.
[19] F.F. Wu, K.C. Chan, S.S. Jiang, S.H. Chen, G. Wang, Sci. Rep. 4 (2014) 5302-5302.
[20] S. Pauly, G. Liu, G. Wang, U. Kühn, N. Mattern, J. Eckert, Acta Mater. 57 (2009) 5445–5453.
[21] Z. Liu, R. Li, G. Liu, K. Song, S. Pauly, T. Zhang, J. Eckert, AIP Adv. 2 (2012) 032176-032176.
[22] K. Kosiba, K. Song, U. Kühn, G. Wang, S. Pauly, Pro. Nat. Sci. Mater. 29 (2019) 576–581.
[23] L. Zhang, S. Pauly, M.Q. Tang, J. Eckert, H.F. Zhang, Sci. Rep. 6 (2016) 19235.
[24] L. Zhang, R.L. Narayan, H.M. Fu, U. Ramamurty, W.R. Li, Y.D. Li, H.F. Zhang, Acta Mater. 168 (2019) 24–36.
[25] H. Matsumoto, S. Watanabe, N. Masahashi, S. Hanada, Metall. Mater. Trans. 37 (2006) 3239–3249.
[26] T. Ozaki, H. Matsumoto, S. Watanabe, S. Hanada, Mater. Trans. 45 (2004) 2776–2779.
[27] K. Kosiba, S. Pauly, Sci. Rep. 7 (2017) 2151.
[28] K. Kosiba, S. Scudino, U. Kühn, A.L. Greer, J. Eckert, S. Pauly, Acta Mater. 127 (2017) 416–425.
[29] S.L. Zhu, X.M. Wang, A. Inoue, Intermetallics 16 (2008) 1031–1035.
[30] F.X. Qin, X.M. Wang, A. Inoue, Intermetallics 15 (2007) 1337–1342.
[31] K. Kosiba, P. Gargarella, S. Pauly, U. Kühn, J. Eckert, J. Appl. Phys. 113 (2013) 123505.
[32] R.M. Srivastava, J. Eckert, W. Löser, B.K. Dhindaw, L. Schultz, Mater. Trans., JIM 43 (2002) 1670-1670.
[33] T. Egami, Prog. Mater. Sci. 56 (2011) 637–653.
[34] T. Egami, S.J.L. Billinge, Structure of amorphous materials, Pergamon 16 (2012) 455–465.
[35] S.V. Ketov, Y.H. Sun, S. Nachum, Z. Lu, A. Checchi, A.R. Beraldin, H.Y. Bai, W.H. Wang, D.V. Louzguine-Luzgin, M.A. Carpenter, A.L. Greer, Nature 524 (2015) 200–203.
[36] Ti_3Cu_4 (Cu_4Ti_3) crystal structure: datasheet from "PAULING FILE multinaries edition " in SpringerMaterials, Springer-Verlag Berlin Heidelberg & Material Phases Data System (MPDS), Switzerland & National Institute for Materials Science (NIMS), Japan, 2012, https://materials.springer.com/isp/crystallographic/docs/sd_1250714.
[37] Ti_2Pd crystal structure: datasheet from "PAULING FILE multinaries edition " in SpringerMaterials, Springer-Verlag Berlin Heidelberg & Material Phases Data System (MPDS), Switzerland & National Institute for Materials Science (NIMS), Japan, 2012, https://materials.springer.com/isp/crystallographic/docs/sd_0261584.
[38] Ti_2Pd_3 crystal structure: datasheet from "PAULING FILE multinaries edition – "in SpringerMaterials, Springer-Verlag Berlin Heidelberg & Material Phases Data System (MPDS), Switzerland & National Institute for Materials Science (NIMS), Japan, 2012, https://materials.springer.com/isp/crystallographic/docs/sd_1251714.
[39] Y. Wang, K. Lu, J. Mater. Sci. Technol. 18 (2002) 492–496.
[40] J. Guo, F. Zu, Z. Chen, S. Zheng, Y. Yuan, Solid State Commun. 135 (2005) 103–107.
[41] W.L. Johnson, G. Kaltenboeck, M.D. Demetriou, J.P. Schramm, X. Liu, K. Samwer, C.P. Kim, D.C. Hofmann, Science 332 (2011) 828–833.
[42] A.J. Drehman, A.L. Greer, Acta Metall. 32 (1984) 323-323.
[43] A.L. Greer, Acta Metall. 30 (1982) 171–192.
[44] A.L. Greer, Metall. Mater. Trans. 27 (1996) 549–555.
[45] D.M. Herlach, Mater. Sci. Eng. R. 12 (1994) 177-177.
[46] A.L. Greer, Nature 366 (1993) 303–304.
[47] K. Kosiba, D. Sopu, S. Scudino, L. Zhang, J. Bednarcik, S. Pauly, Int. J. Plast. 119 (2018) 156–170.
[48] A. van den Beukel, J. Sietsma, Acta Metall. Mater. 38 (1990) 383–389.
[49] B. Sarac, L. Zhang, K. Kosiba, S. Pauly, M. Stoica, J. Eckert, Sci. Rep. 6 (2016) 27271.
[50] M. Wakeda, J. Saida, J. Li, S. Ogata, Sci. Rep. 5 (2015) 10545.
[51] S. Küchemann, P.M. Derlet, C. Liu, D. Rosenthal, G. Sparks, W.S. Larson, R. Maaß, Adv. Funct. Mater. 28 (2018) 1805385.